Topographical and Microstructural Effects of Laser Surface Texturing on Tin-Coated Copper Electrical Connectors Under Load Cycling

K. E. Trinh, E. Ramos-Moore, I. Green, C. Pauly, M. Zamanzade, and F. Mücklich

***Abstract*— Increasing demands on modern connector materials for automotive applications, driven by the trends in miniaturization and electrification, require higher operating temperatures and lower contact normal loads. These lead to increased wear, begging the need for upgraded connector materials. In order to improve the electrical and wear behavior of an existing surface finish, the use of direct laser interference patterning (DLIP) on tin-plated copper contacts is explored. The focus of this paper lies on the evolution of the electrical resistance between textured contacts and a probe with an inert coating under normal loading. The microstructural and topographical changes due to DLIP as well as indentation during the contact resistance measurement are investigated by white light interferometry, scanning electron microscopy, and focused ion beam. The patterns change the primary deformation mechanism of the connector surface, which facilitates the fracture of electrically insulating oxide layers. This in turn leads to a decreased contact resistance in the considered load range, compared to the nontextured samples.**

***Index Terms*— Automotive materials, connectors, contact resistance, microstructure, surface engineering, surface texture, surface topography.**

I. INTRODUCTION

AN ELECTRICAL connector must provide a separable interface between two electronic systems. Most importantly, modern connectors must do so with a low and constant electrical contact resistance (ECR), while being highly wear-resistant. Especially in the automotive industry, installation and maintenance require manual connector manipulation and therefore low and stable insertion and withdrawal forces. Driven by the trends in miniaturization and higher voltage applications, the operating conditions will intensify in the near future [1], [2]. Common nonnoble materials for surface finishes, especially tin, have to meet these increasingly higher standards. Due to cost reasons, tin cannot be replaced by noble metals in the mass market, and therefore new solutions to improve tin-based material systems are required. Tin is susceptible to fretting wear, caused by vibrations or thermal cycling during service, as well as sliding wear during mating and unmating [3].

Laser surface texturing (LST) is an advanced technique that provides control of the wear behavior of sliding metal surfaces. It can be used to create surface cavities, which reduces the adhesion between the surfaces and acts as traps for wear debris produced during fretting, thus hindering the formation of an insulation layer between contacting surfaces [4]. One special form of LST is the so-called direct laser interference patterning (DLIP) [5]. Its main advantage is that the periodic surface textures in the micrometer range can be created instantly in one laser shot (texturing speed up to several cm^2/s) [6], [7]. Although texturing can improve the mechanical wear resistance of surfaces, its influence on the ECR is still unknown. Myers *et al.* [8], [9] and Leidner *et al.* [10] showed that maximal current density and maximal von Mises stress in a Hertzian contact are typically not coincident. By creating a nonconformal contact, they were able to achieve a congruent mechanical and electrical distribution. As an example, they simulated a contact between a metallic half-sphere and a flat metallic surface with a sinusoidal grove texture with periodicities between 14 and 4150 μm. According to their simulations, a smaller periodicity leads to a larger reduction of the ECR. They suggested that periodicities between 200 and 500 μm are optimal since smaller textures, although more beneficial, entail problematic fabrication by conventional coining with subsequent coating. Laser interference patterns, with features well below 20 μm achievable in a single step, emerge as an interesting approach for such applications. The beneficial effect of DLIP on the ECR as a function of the applied normal load has been pointed out in [11]. In a single loading/unloading cycle experiment, it was shown that the native oxide layer on the tin surface more readily breaks on a textured surface, compared to a conventional surface finish, leading to a higher conductivity through the contact interface.

This paper addresses the topographic and microstructural changes occurring during ECR measurements of DLIP-textured/nontextured tin-plated copper contacts under

Manuscript received October 29, 2015; revised June 2, 2016 and September 18, 2016; accepted December 23, 2016. Date of publication February 24, 2017; date of current version April 18, 2017. This work was supported in part by the European Commission under project Fondecyt 11121630, Chile, in part by EFRE under AME-Laboratory project, and in part by IRSES under Project 318903. Recommended for publication by Associate Editor J. McBride upon evaluation of reviewers' comments.

K. E. Trinh and F. Mücklich are with the Institute of Functional Materials, Saarland University, 66121 Saarbrücken, Germany, and also with the Materials Engineering Center Saarland, 66123 Saarbrücken, Germany (e-mail: k.trinh@mx.uni-saarland.de).

E. Ramos-Moore is with the Facultad de Física, Pontificia Universidad Católica de Chile, Santiago 7820436, Chile.

I. Green is with the Woodruff School of Mechanical Engineering, Georgia Institute of Technology, Atlanta, GA 30332 USA.

C. Pauly is with the Institute of Functional Materials, Saarland University, 66121 Saarbrücken, Germany.

M. Zamanzade is with the Institute of Materials Science and Methods, Saarland University, 66121 Saarbrücken, Germany.

Color versions of one or more of the figures in this paper are available online at http://ieeexplore.ieee.org.

Digital Object Identifier 10.1109/TCPMT.2017.2659224

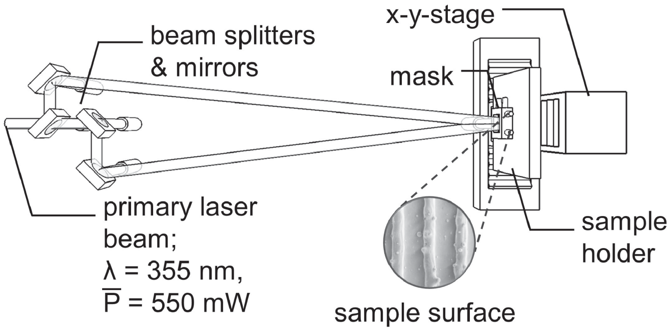

Fig. 1. Schematic of a two-beam laser interference setup. The primary beam is split into two individual sub-beams, which interfere at the sample surface. The interference patterning was done with a wavelength of 355 nm and a mean power of 550 mW. Inlay zoom: SEM image of metallic textured surface.

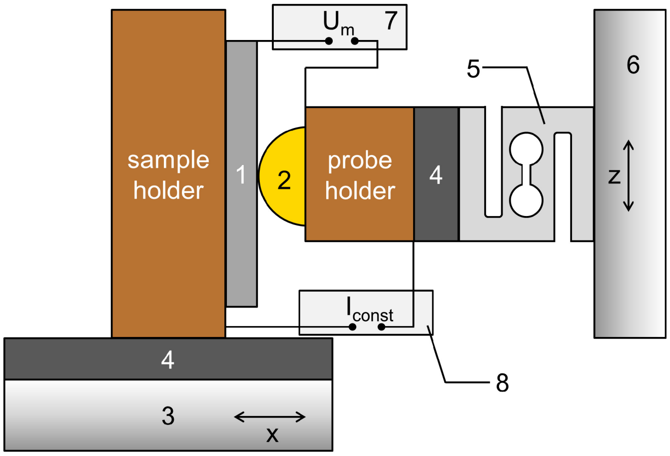

Fig. 2. Schematic of the contact resistance measurement test rig. 1—sample, 2—probe, 3—piezo stage, 4—electrical insulation, 5—force sensor, 6—cross table, 7—nanovoltmeter, and 8—source meter [31].

cyclic loading conditions. The roles of the textures on these changes and those of the ECR are studied. The evolution of the contact resistance is measured as a function of the normal load upon a hemispherical counterpart probe. The topography and microstructure are analyzed using white light interferometry (WLI), scanning electron microscopy (SEM), focused ion beam (FIB), energy-dispersive X-ray spectroscopy (EDS), electron backscatter diffraction (EBSD), and nanoindentation.

II. EXPERIMENTAL METHODS

A. Sample Preparation and Direct Laser Interference Patterning

The studied samples are hot-dipped tin-plated copper sheets with a total thickness of 280 μm. All samples were cleaned in an ultrasonic bath with acetone, followed by isopropanol and distilled water, prior to the texturing process. Samples were mounted on a motorized precision *XY* stage. A mask was used to select a rectangular area from the circular beam profile in order to precisely irradiate the sample surface.

The surface texture was produced by interfering laser beams (Fig. 1) with DLIP [12]. A single 10-ns pulse from the primary beam of a pulsed Nd:YAG laser (Spectra Physics Quanta-Ray Pro 290) is split into two or more sub-beams. In this paper, three beam interferences were used to produce a hexagonal surface topography.

B. Topography, Chemistry, and Microstructure Characterization

Samples were cleaned in an ultrasonic bath using acetone, isopropanol, and distilled water prior to the measurements, without any further surface treatment. The surface topography of the samples before and after texturing was measured by a white light interferometer (Zygo New View 7300) with a vertical resolution below 0.1 nm. The 3-D data measured with this technique allow access to a number of surface parameters like roughness and periodicity of the laser-textured samples.

A SEM/FIB dual-beam workstation (FEI Helios NanoLab 600) equipped with EBSD/EDS detectors (EDAX) was used to conduct topographic, cross-sectional, and elemental analyses of nontextured and textured samples. The cross sections were created by FIB ion milling. The EBSD measurements were performed using a voltage of 20 kV, a current of 22 nA, and a step size of 0.5 μm, and grains were segmented at a minimum boundary misorientation of 2°. The unfiltered raw data were used to create EBSD maps.

C. Hardness Measurement

The hardness and elastic modulus (E-modulus) of the nontextured samples were measured with a Hysitron TI 900 TriboIndenter equipped with a nanoDMA III compatible transducer and a sharp Berkovich diamond tip. The measured tip radius was 270 nm. The indentation depth was set to be 100 nm, less than 10% of the tin layer thickness.

Because of the high roughness of the textured surfaces (R_a: 505 ± 43 nm), nanoindentation with a sharp tip could not deliver meaningful results. Hence, in order to qualitatively compare the mechanical properties of both sample types, an ASMEC UNAT-SEM II nanoindenter with a spherical steel tip having a 0.75-mm radius was used. This nanoindenter was installed in a SEM (Zeiss Sigma VP) in order to make *in situ* indentation at defined positions. A normal load of 170 mN leads to contact pressure magnitudes similar to those observed in the contact resistance measurements (~500 N/mm^2). Further description of the method can be found elsewhere [13].

D. Measurement of the Electrical Contact Resistance

The measurement of the ECR was done with a self-built test rig, which works according to the four-wire method (Fig. 2). A defined point contact is created between the sample (1 in Fig. 2) and a probe (2), both electrically insulated (4) from their respective holders. The probe is a sphere with a radius of 4000 μm made of a silver alloy, covered with a 5-μm-thick inert gold coating. The mean roughness R_a of the sphere is 267 ±50 nm. The normal load is applied by a linear piezo drive (3) with a lateral resolution of 0.1 μm. The load is measured by a force sensor (5) with a resolution of 0.02 N. Probe positioning is done by a manual cross table (6).

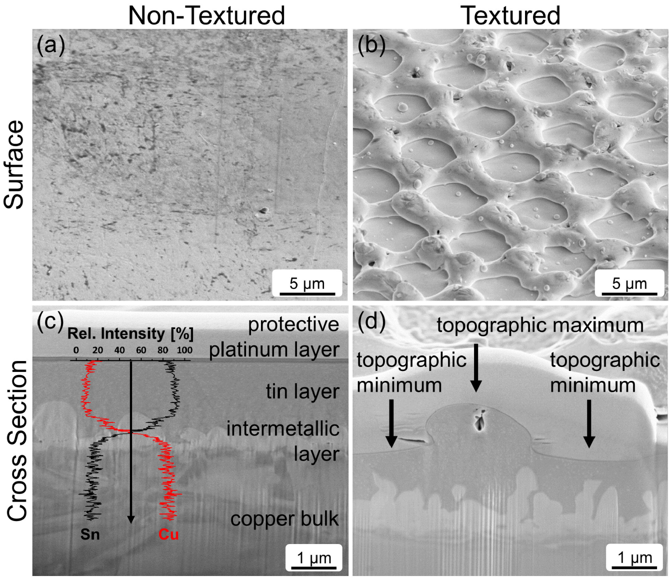

Fig. 3. SEM images of hot tin-dipped copper samples. Surface (top row, 52° viewing angle) and cross-sectional (bottom row) views. (a) and (c) Nontextured. (b) and (d) Textured samples. In (c), EDS linescans are included in order to identify the chemical composition of the samples [32].

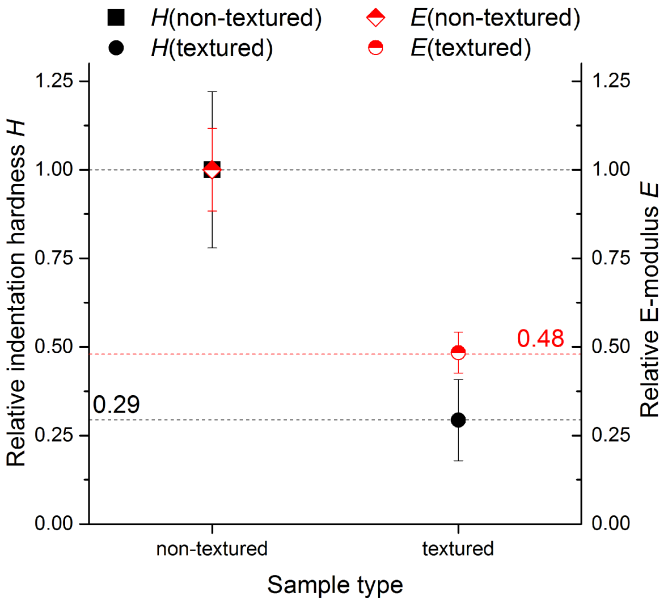

Fig. 4. Relative hardness and relative E-modulus of the nontextured and textured samples (microindentation measurements). The results have been normalized to the corresponding value of the nontextured reference.

Through a first set of leads, a constant current (I_{const}) is applied between the sample and the probe from a current source meter Keithley 2400 (7) with an accuracy of 200 nA. Through a second set of leads, the voltage drop U_m between probe and sample is measured by a nanovoltmeter Keithley 2182a (8) with a resolution of 10 nV. All measurements were done under dry conditions (current $<$ 100 mA and open circuit voltage $<$20 mV) to prevent damaging of any existing surface layers. Further description of the test setup can be found elsewhere [11].

Statistical error bars were estimated for each load by measuring five different points within each sample under the same experimental conditions. The textured and nontextured samples were measured in a load range between 1.6 and 10 N for 15 complete loading/unloading cycles. The relatively high starting load of 1.6 N was applied in order to assure a stable mechanical contact during testing.

III. RESULTS AND ANALYSIS

A. Direct Laser Interference Patterning

DLIP produces periodic intensity variations from at least two (three in this case) laser beams that interfere at the sample surface. Strong temperature gradients ensue between the intensity maxima, with temperatures in the thousands of degrees (°C), and the minima, one order of magnitude lower. According to simulations based on [14], this gradient can reach 370 °C/μm. The surface tension gradient induced by the large temperature difference causes a liquid flow from the warmer to the cooler regions. In combination with a cooling rate of up to 10^{10} K/s, this leads to a residual periodic surface topography after resolidification of the irradiated material [15]–[17].

The sample surfaces before and after texturing as well as their respective cross sections are presented in Fig. 3. The mean roughness R_a of the nontextured sample [Fig. 3(a)], as determined by WLI measurements, is 10 ± 1 nm. After texturing, a strong hexagonal topography with a periodicity of 7.5 μm is observed [Fig. 3(b)]. In addition to the actual texture, small resolidified tin droplets can be observed on top of the surface. During texturing, these droplets are ejected from the surface when colliding fronts of molten tin meet, on their stated displacement from hot (laser intensity maxima) to cold (minima) regions.

Cross-sectional images show that the tin-layer thickness is around 2 μm before texturing [Fig. 3(c)]. Between the bulk material and the surface layer, there is also an intermetallic layer consisting of copper and tin [Fig. 3(c), EDS linescan]. This kind of layer consists of an upper Cu_6Sn_5 and a lower Cu_3Sn sublayer [9]–[13]. DLIP leads to a periodic variation of the tin layer thickness [Fig. 3(d)]. The mean peak-to-valley roughness R_{tm} measured by WLI is 1.8 μm. It is worth noting that the texturing did not lead to a total penetration of the tin coating. Indeed, the intermetallic layer was fully intact after laser irradiation. Some pores are visible at the topographic maxima, which were created during the resolidification of the molten tin.

The nanoindentation showed that the hardness and the E-modulus of the nontextured tin layer are 0.53 ± 0.11 and 39.4 ± 3.6 GPa, respectively. These values are in agreement with those derived in [18].

The results of the comparative study with the microindenter are shown in Fig. 4. As can be seen, DLIP leads to an apparent reduction in hardness of about 71% and a reduction of the E-modulus of about 52%. It should be emphasized that the observed changes of hardness and modulus of the textured surface are probably not due to an actual change of the material's properties but mainly caused by the enhanced plastic flow in the contact area. The topography leads to higher contact pressure (as simulated in [31]) and facilitates plastic flow due to the presence of well-arranged topographic maxima and minima. The measured values therefore represent a combination of the material's properties and the periodic DLIP patterning. By comparison with the results of the nontextured surface, the influence of DLIP on the "mechanical reply" of the sample to the given load is shown.

Using the topographical data from WLI measurements together with the mechanical analyses, the calculation of the plasticity index ψ, introduced in [19], is possible according to [20]

$$\psi = \frac{E'}{H}\sqrt{\frac{R_{\mathrm{rms}}}{R}} \tag{1}$$

where H is the hardness, R_{rms} is the root-mean-square roughness, R is the reciprocal of the mean curvature of the highest asperities, defined as the mean asperity radius of curvature, and $E'$is the effective modulus of elasticity.

E' is defined as

$$\frac{1}{E'} = \frac{1-\nu_1^2}{E_1} + \frac{1-\nu_2^2}{E_2} \tag{2}$$

where $\nu_{1/2}$ is the Poisson ratio and $E_{1/2}$ is the elastic modulus of tin and the tip, respectively. The plasticity index can be interpreted as a measure of the critical pressure for transition from elastic ($\psi < 0.6$) to plastic ($\psi > 1$) deformation of the mechanical contact [19].

From (1) and (2), the respective plasticity indexes of the nontextured and textured samples are 0.20 ± 0.05 and 43.54 ± 10.12. According to the theory in [19], the textured sample should thus deform plastically at lower loads than the nontextured sample.

B. Electrical Resistance Measurements

The ECR as a function of the normal load during 15 loading cycles is shown in Fig. 5(a). The contact resistance of the textured samples is lower than that of the nontextured sample over the whole load range and for all cycles. For both samples, the ECR drops in the first cycle during loading and increases again during unloading, without reaching the initial resistance value (i.e., hysteresis). The scattering of the results is also reduced after the first loading. In the subsequent cycles, the variation of the resistance as a function of the load became less pronounced. For the nontextured samples, the difference in ECR between the initial load of 1.6 N and the maximum load of 10 N is about 1.44 mΩ in the first cycle, whereas after 15 cycles, no significant difference is observed. DLIP weakens the load dependence of the ECR: after a 0.22-mΩ difference in the first cycle, no significant difference was observed for the remaining 15 cycles.

It is worth noting that the hysteresis (ΔECR) between each cycle is significantly smaller in the textured case, at least in the early stage of the experiments. For the nontextured sample, $\Delta ECR(1.6\ \mathrm{N})$ is 1.01 mΩ after one cycle and negligible compared to the measurement error (~0.05 mΩ) after 15 cycles. After texturing, the hysteresis gap of the contact resistance is negligible compared to the measurement error.

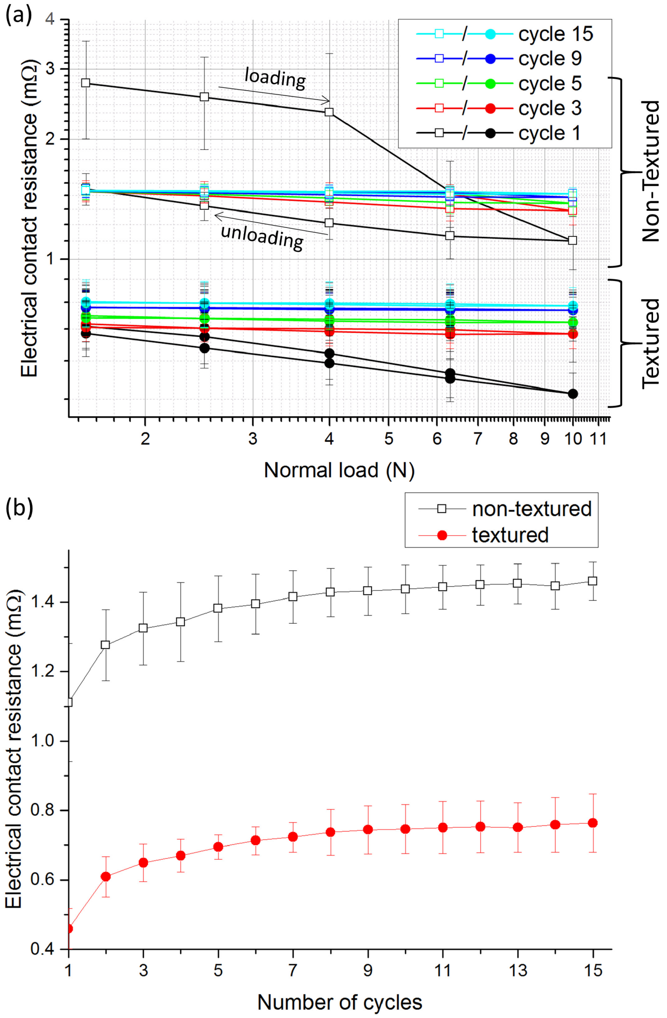

Fig. 5. (a) ECR as a function of normal load (double logarithmic scale); 15 complete cycles of the nontextured sample (☐) are compared to the textured sample (●). Shown are only cycles 1, 3, 5, 9, and 15 for better overview. (b) Evolution of the ECR Rc of nontextured (☐) and textured (●) samples at a normal load of 10 N.

It can also be observed that the contact resistance increases from cycle to cycle (at maximal load), after the first cycle. However, this tendency slows with subsequent cycling. In particular, this evolution of the intercycle contact resistance with subsequent cycling was further investigated for a normal load of 10 N [Fig. 5(b)]. For both samples, the contact resistance initially increased steeply, yet further cycles smoothly flattened out the curve. The ECR of the nontextured samples is significantly higher than that of the textured samples during the complete cycling interval. The ratio ECR(nontextured)/ECR(textured) has an initial value of 2.4 and drops to 1.9 after 15 cycles.

C. Microstructural Modification of the Contact Surface

1) One ECR Measurement Cycle: In order to understand the behavior of the contact area during the measurements, the surface topography of the nontextured and textured samples after one measurement cycle with 10 N was studied by SEM and WLI (Fig. 6). The nontextured surface [Fig. 6(a) and (c)]

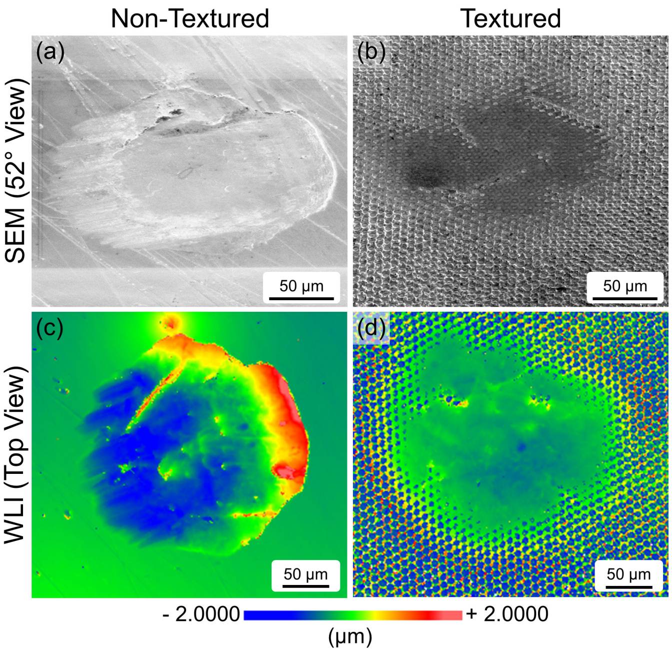

Fig. 6. SEM (top row, 52° viewing angle) and WLI (bottom) images of (a) and (c) nontextured and (b) and (d) textured sample surfaces after the first cycle of the electrical contact resistant measurements with a maximum normal load of 10 N. The sphere radius of the probe was 4000 μm.

presented an inhomogeneous topography. On the left side of the indent, wear scars are visible, as well as material pile up directly opposite, indicating slight sphere drift, possibly due to a minimal perpendicularity default. Furthermore, since the probes are not perfectly spherical, they embossed their own topography on the flat samples. These effects are less severe in the textured surface [Fig. 6(b) and (d)]. Instead, the plastic deformation caused a material to flow from the topographic maxima to the minima, filling up the dimples and flattening the sample at the center of the indent.

The microstructural evolution of a nontextured sample, after one cycle of varying maximal loads (0.25–10 N, each on a different location), is presented in EBSD inverse pole figure (IPF) maps integrated with image quality (IQ) (Fig. 7). Even if no stable mechanical or electrical contact could be achieved at normal loads smaller than 1.6 N, the load range from 0.25 to 1.0 N was also taken into account to study the microstructural changes in the indentation zone. The initial grains [Fig. 7(a)] are strongly elongated, caused by the manufacturing process, and contain many subgrain boundaries. Here, the material already shows signs of plastic deformation, at 0.25 N [Fig. 7(a)], whereas significant crystallographic changes start at 0.63 N. The new grains in the indentation zone are due to plastic deformation and dynamic recrystallization (DRX) processes, much more significant at higher loads. DRX can take place at half of the absolute melting temperature T_m [$T_m(\mathrm{Sn}) = 505.08$ K] [21]. Above 0.63 N, the grain size in the plastically deformed area decreases drastically.

The EBSD measurements of the textured surface did not lead to satisfying diffraction patterns due to a shadowing effect at low loads. The steep topography blocked most of the backscatter signal in the topographic minima and some zones of the maxima. Therefore, meaningful EBSD data could be recorded only for samples tested at normal loads of 10 N (see Fig. 8). The contact area contains a large amount of moderate deformation with flattened topographic maxima as well as two elliptic regions of stronger deformation where grain refinement is easily identified in the IPF map [Fig. 8(a)]. To see whether DLIP itself has an effect on the grain size, an orientation from the moderately deformed center region of the contact area was randomly selected and all data points within a 10° tolerance have been highlighted [Fig. 8(b)]. The tolerance of 10° was chosen to account for the large orientation gradients in the elongated grains of the as-received samples

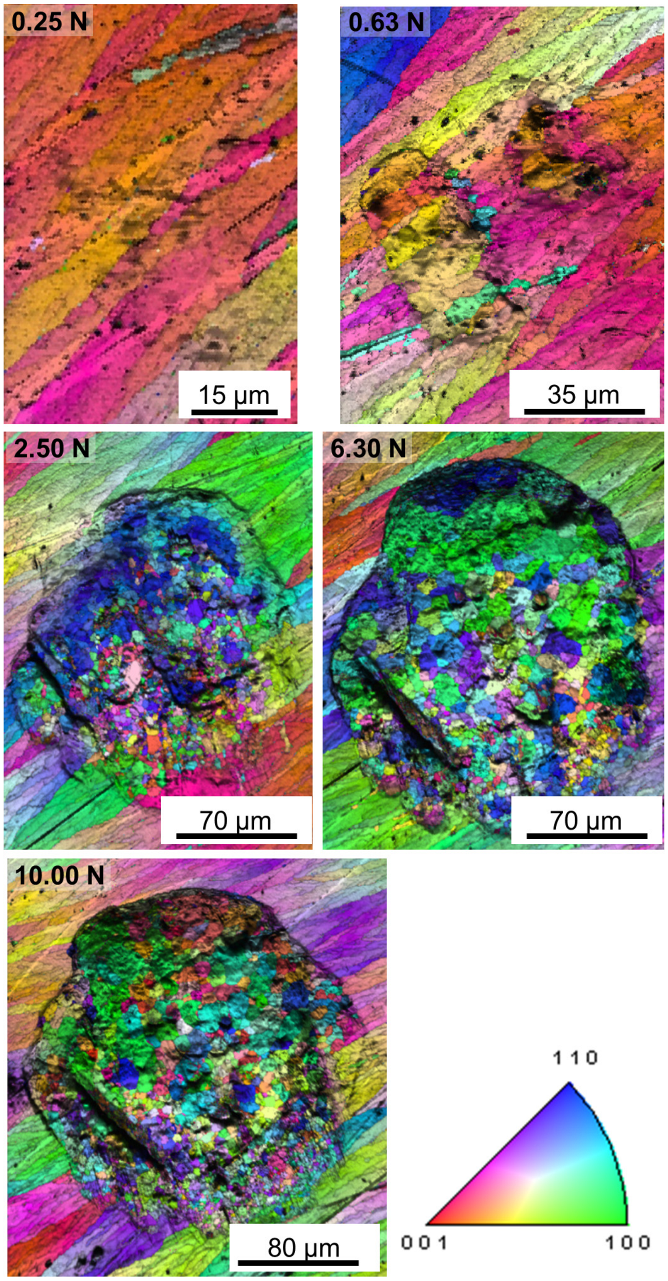

Fig. 7. EBSD maps of IPF integrated with IQ of the nontextured samples after the electrical contact resistant measurements under different normal loads.

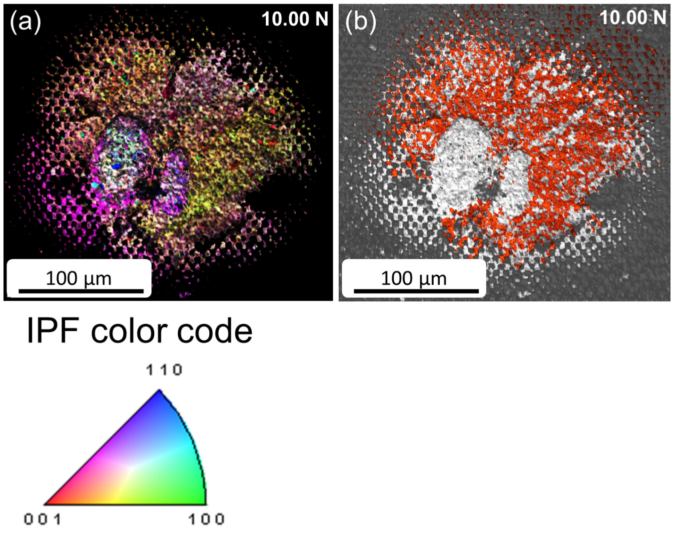

Fig. 8. Textured sample after the electrical contact resistance measurements under a normal load of 10 N. (a) EBSD maps of IPF integrated with IQ. (b) Grain orientation (color) and IQ value (gray scale) map. An orientation from the center (a) was randomly chosen, and all points within a 10° tolerance were given the same color, resulting in a continuous area.

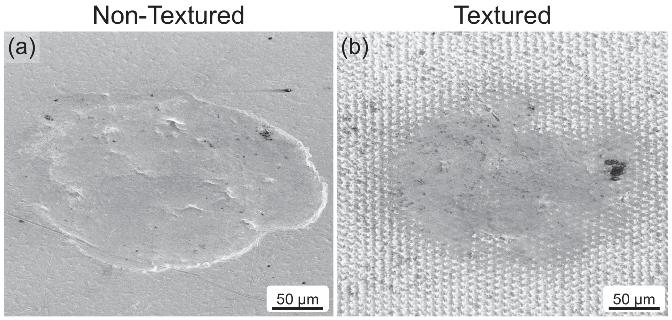

Fig. 9. SEM images of (a) nontextured and (b) textured surfaces after 15 cycles of contact resistance measurements (measured in a position other than shown in Fig. 6).

as can be seen in the undeformed regions in Fig. 7(a). This led to a continuous area, significantly larger than the pattern periodicity. Local discontinuities are either due to shadowing or smaller grains that have formed in the more deformed topographic maxima. In contrast to the moderately deformed region, the elliptic regions of strong deformation in Fig. 8 show small equiaxed grains that do not share the selected orientation. In accordance with the results obtained for the nontextured samples, the grain refinement is induced by DRX due to plastic deformation but not by DLIP itself.

2) Fifteen ECR Measurement Cycles: The surfaces of the nontextured and textured indents after 15 cycles of contact resistance measurement are shown in Fig. 9. The shape and diameter of the imprints are comparable to those after the first cycle (Fig. 6). However, no wear scars are visible on the nontextured sample. The textured sample presents a progressively flattened pattern toward the center, where no features remain.

The profile of the surface before and after ECR measurement was studied by WLI (Fig. 10). The material piled up is clearly visible on the nontextured surface after the first cycle [Fig. 10(c)]. The shape of the profile does not change significantly after 15 cycles [Fig. 10(e)]. In contrast, material sink-in can be observed in the textured sample Fig. 10(d), where the topographic maxima have flowed into the minima, leading to flattening after the first cycle. Subsequent cycling slightly widens this effect [Fig. 10(f)].

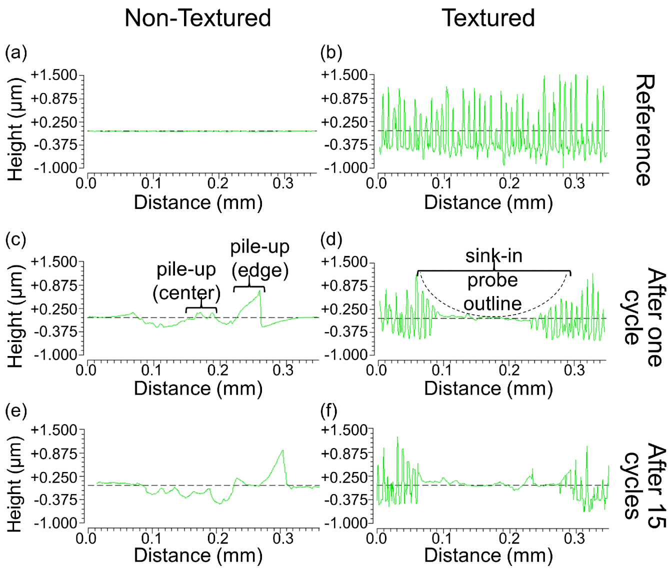

Fig. 10. Depth profiles obtained by WLI of the surface of nontextured (left) and textured (right) samples. (a) and (b) Before the contact resistance measurements. (c) and (d) After the first indentation. (e) and (f) After 15 indentation cycles. In (c) and (d), pile-up and sink-in effects on the samples are observed after indentations using the hemispherical probe.

As can be seen in Fig. 7, plastic deformation of the nontextured samples starts already at loads of 0.25 N, corresponding to a Hertzian pressure of 153.4 MPa. This indicates that the critical load is already exceeded. Nevertheless, with the WLI profiles, it may be concluded that the textured sample deforms stronger at a given load than the nontexured sample, confirming the plasticity index tendency.

IV. DISCUSSION

The load-dependent behavior of the ECR of the first cycle has been discussed in [11]. It was found that the total ECR of the textured sample is determined by the constriction resistance. The resistance–load dependence revealed that plastic deformation dominates over the whole load range. However, on the nontextured sample, the contact resistance is influenced by contributions from constriction as well as film resistance. No single deformation mechanism dominated over the whole load range. This also holds true for this paper, although the absolute values of the slope n of the resistance–load curves deviate from the original study. For normal loads between 1.60 and 4.00 N, the curve of the nontextured sample has a slope of -0.184 ± 0.002 compared to -0.631 ± 0.032 in the original study. The deviation is smaller for loads >4 N [$n(present) = -0.714 \pm 0.114$ and $n(original) = -0.863 \pm 0.099$]. The difference in absolute values indicates a dependence of the resistance-load behavior on the

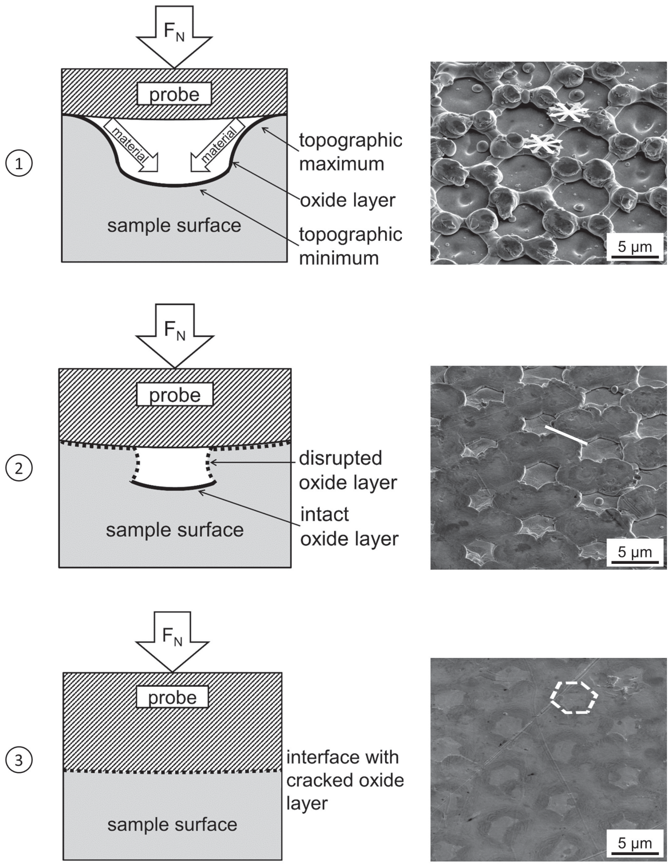

Fig. 11. Deformation model of the laser-textured sample under normal loading. Left: schematic cross sections. Right: SEM images of the surface (observation angle 52°). (1) First contact between probe and sample. (2) Material flow from topographic maxima to minima. Flattening of the surface pattern and disruption of the oxide layer. (3) Surface after loading with 10 N: topographic minima are filled with material from the maxima based on [32].

load ramping conditions. In the original study, the ECR measurements started at an initial load of 0.25 N, followed by measurements at 0.40, 0.63, and 1.00 N before reaching the level of 1.6 N (corresponding to the initial load in this paper). Since every measurement step takes approximately 4 min, additional measurements in the low load regime allow more time for relaxation processes, which can influence the deformation behavior of the sample surfaces. However, a systematic investigation of this effect is beyond the scope of this paper and should be studied separately.

Based upon topographic and microstructural observations, the following model is proposed to describe deformation of the textured surfaces. When the probe touches the textured sample surface, the applied load acts on the topographic maxima (Fig. 11, step 1). Compared to the nontextured surface, the textured surface has a lower real area of contact, thus leading to higher local surface pressures in the topographic maxima. This is in accordance with the calculated plasticity indices, which are two orders of magnitude higher on the textured samples. At higher loads, the topographic maxima are flattened and a radial material flow sets in (Fig. 11, step 2). During this deformation process, the oxide layer on the sample surface is disrupted, resulting in a decreased ECR. The material flow leads to the formation of new interfaces between the former topographic maxima (Fig. 11, step 2, right). After this interface formation, the material flows to the topographic minima under further loading until they are totally filled (Fig. 11, step 3). A flat conducting interface is formed between the probe and the sample. The described oxide layer disruption explains why the contribution of the film resistance to the total ECR of the textured samples is small, compared to the contribution of the constriction resistance as stated in [11].

From the EBSD results, it can be seen that new grains are formed in the first cycle (Figs. 7 and 8). On the nontextured samples, the grain refinement happens at a load of 0.63 N as a result of DRX. Since the topography on the textured samples blocked the EBSD signal at low loads, DRX was observable only after loading with 10 N. In the case of tin, T_m is 505.08 K, which means that DRX can occur at room temperature [21]. The formation of new grains enhances the density of grain boundaries, hence reducing the dislocation density. This density can be reduced in metals by up to six orders of magnitude due to DRX (from 10^{16} to 10^{10} m^{-2}) [22]. This may also influence the electrical resistivity of the material. Following the Matthiessen rule, the resistivity ρ of metals is:

$$\rho = \rho_{\mathrm{th}} + \rho_{\mathrm{imp}} + \rho_{\mathrm{def}} \tag{3}$$

where ρ_{th} is the thermal contribution, ρ_{imp} is the contribution by impurities, and ρ_{def} is the contribution by defects (e.g., dislocations).

The change in dislocation density was not measured in the frame of this paper. Nevertheless, from studies of other metals, like copper [23], [24], iron [25], as well as aluminum and nickel [26], it is known that a change in dislocation density can lead to a change in resistivity in the single-digit percent range. The contribution of such a change to the ECR is negligible compared to the influence of the native oxide layer since the resistivity of tin oxide is about six orders of magnitude higher than that of metallic tin [27], [28].

A change in grain boundary density may also influence the ECR. This holds true only if the grain diameter is in the order of the mean free path of electrons [29]. For tin, the mean free path is 8.3 nm, which is about three orders of magnitude smaller than the grain size of the newly formed grains. Consequently, a contribution from the grain boundaries to the contact resistance can be neglected.

The discussion shows that the main contribution of DLIP to the reduction of the ECR originates from the changed deformation mechanism, facilitating the disruption of the surface oxide layer (see Fig. 11).

Regarding the effects of cyclic loading on the contact resistance, the results show changes in the load-dependent contact resistance behavior. With increasing cycle number, the following general observations have been made for both the nontextured and the textured surfaces.

1) The contact resistance rises.
2) The load-dependence becomes weaker.
3) The hysteresis decreases.

In the first cycle, the real area of contact increases during loading as a consequence of elastic and plastic deformation.

During unloading, the contact area decreases, and therefore ECR rises. This effect weakens in the subsequent cycles, when the surface becomes flattened due to plastic deformation and the contact area changes mainly due to elastic deformation [Figs. 6(a) and (b) and 9]. The plastic deformation of the tin layer is constrained by the underlying intermetallic phase and the copper substrate. A similar behavior has been observed by Tamai *et al*. [30]. They studied the contact resistance of pure tin and tin-coated bronze and found out that the hard bronze substrate constrained the plastic deformation of the tin layer. This led to a smaller hysteresis of the contact resistance between loading and unloading compared to the pure tin samples. Thus, the constrained plastic deformation with subsequent cycling is not only responsible for the weakening of the load-dependence, but also for the decrease in the hysteresis.

The rising contact resistance from cycle to cycle may be attributed to a misalignment between probe and sample, deviating from a perfect 90° angle. As can be seen in Fig. 6, the probe slides over the sample surface leaving scratches. This decreases the real area of contact and increases the contact resistance. This effect becomes weaker when the indented area is flattened during subsequent cycling, which might be an explanation for the flattening of the curves shown in Fig. 5(b).

Comparing the two samples, it is visible that the contact resistance of the laser-textured sample stays below the nontextured reference even after 15 cycles (Fig. 5). As described earlier in this section, the oxide layer is disrupted in the first cycle of the experiment (Fig. 11). In the subsequent cycles, the normal load was varied between 1.6 and 10 N maintaining the mechanical contact (at least) in the center of the indent during the whole experiment. As a consequence, the tin surface was sealed from the atmosphere in this region, thus inhibiting the formation of a new oxide layer in the center of the indent. Therefore, the beneficial effect of the texture achieved in the first cycle was preserved for the duration of the whole experiment.

V. CONCLUSION

Our findings show that the observed microstructural changes (grain refinement) have little effect on the load-dependent ECR behavior, compared to that of the changed deformation behavior induced by DLIP. Thus, the reduction of the ECR (up to 58% at a normal load of 10 N) and its hysteresis between the first loading/unloading cycle can be ascribed to the higher plasticity of the laser-textured surface and hence to an easier disruption of the native surface oxide layer compared to the flat nontextured surface. Moreover, the cyclic loading measurements show that with increasing cycles, the ECR rises and becomes less dependent on the load, and its hysteresis between loading and unloading decreases.

ACKNOWLEDGMENT

K. E. Trinh would like to thank W. Ott, S. Slawik, and B. Schroeder for their support in the development of the contact resistance test rig. He would also like to thank N. Souza and F. Lasserre for proofreading.

REFERENCES

[1] Y. W. Park, T. S. N. S. Narayanan, and K. Y. Lee, "Fretting corrosion of tin-plated contacts: Evaluation of surface characteristics," *Tribol. Int.*, vol. 40, no. 3, pp. 548–559, 2007.

[2] I. Buresch and F. Bubeck, "Contact resistance, formability and strength optimizing all parameters in fine grain bronzes for connector applications," in *Proc. 24th Int. Conf. Elect. Contacts*, Saint-Malo, France, 2008, pp. 192–198.

[3] M. Antler, "Sliding wear of metallic contacts," *IEEE Trans. Compon., Hybrids, Manuf. Technol.*, vol. 4, no. 1, pp. 15–29, Mar. 1981.

[4] I. Etsion, "State of the art in laser surface texturing," *J. Tribol.*, vol. 127, no. 1, pp. 248–253, 2005.

[5] F. Mücklich, A. Lasagni, and C. Daniel, "Laser interference metallurgy—Using interference as a tool for micro/nano structuring," *Z. Metallkunde*, vol. 97, no. 10, pp. 1337–1344, 2006.

[6] A. F. Lasagni, T. Roch, D. Langheinrich, M. Bieda, and A. Wetzig, "Large area direct fabrication of periodic arrays using interference patterning," *Phys. Procedia*, vol. 12, Part B, pp. 214–220, 2011. [Online]. Available: http://www.sciencedirect.com/science/article/pii/S1875389211002045

[7] A. F. Lasagni *et al.*, "Bringing the direct laser interference patterning method to industry: A one tool-complete solution for surface functionalization," in *Proc. 15th Int. Symp. Laser Precis Microfabrication*, Vilnius, Lithuania, 2014, pp. 340–344.

[8] M. Myers, M. Leidner, and H. Schmidt, "Effect of contact parameters on current density distribution in a contact interface," in *Proc. 57th IEEE Holm Conf. Elect. Contacts*, Minneapolis, MN, USA, Sep. 2011, pp. 1–9.

[9] M. Myers, M. Leidner, H. Schmidt, S. Sachs, and A. Baeumer, "Contact resistance reduction by matching current and mechanical load carrying asperity junctions," in *Proc. 58th IEEE Holm Conf. Elect. Contacts*, Portland, OR, USA, Sep. 2012, pp. 1–8.

[10] M. Leidner, M. Myers, H. Schmidt, S. Sachs, and S. Thoss, "Enhancing the contact interface by matching the surface pressure and current density distribution," in *Proc. 27th Int. Conf. Elect. Contacts*, Dresden, Germany, Jun. 2014, pp. 1–6.

[11] K. E. Trinh, F. Muecklich, and E. Ramos-Moore, "The role of microstructure and surface topography in the electrical behavior of Sn-coated Cu contacts," in *Proc. 27th Int. Conf. Elect. Contacts*, Dresden, Germany, 2014, pp. 243–248.

[12] F. Mücklich, A. Lasagni, and C. Daniel, "Laser interference metallurgy—Periodic surface patterning and formation of intermetallics," *Intermetallics*, vol. 13, pp. 437–442, Mar./Apr. 2005.

[13] M. Zamanzade, H. Vehoff, and A. Barnoush, "Effect of chromium on elastic and plastic deformation of Fe_3Al intermetallics," *Intermetallics*, vol. 41, pp. 28–34, Oct. 2013.

[14] A. Lasagni and F. Mücklich, "FEM simulation of periodical local heating caused by laser interference metallurgy," *J. Mater. Process. Technol.*, vol. 209, pp. 202–209, Jan. 2009.

[15] A. F. Lasagni, "Advanced design of periodical structures by laser interference metallurgy in the micro/nano scale on macroscopic areas," Ph.D. dissertation, Dept. Mater. Sci. Eng., Saarland Univ., Saarbrücken, Germany, 2006.

[16] C. Gachot, "Laser interference metallurgy of metallic surfaces for tribological applications," Ph.D. dissertation, Dept. Mater. Sci. Eng., Saarland Univ., Saarbrücken, Germany, 2012.

[17] T. D. Bennett, D. J. Krajnovich, C. P. Grigoropoulos, P. Baumgart, and A. C. Tam, "Marangoni mechanism in pulsed laser texturing of magnetic disk substrates," *J. Heat Transf.*, vol. 119, no. 3, pp. 589–596, 1997.

[18] X. Deng, N. Chawla, K. Chawla, and M. Koopman, "Deformation behavior of (Cu, Ag)–Sn intermetallics by nanoindentation," *Acta Mater.*, vol. 52, pp. 4291–4303, Aug. 2004.

[19] J. A. Greenwood and J. B. P. Williamson, "Contact of nominally flat surfaces," *Proc. R. Soc. Lond. A, Math. Phys. Sci.*, vol. 295, no. 1442, pp. 300–319, 1966.

[20] B.-G. Rosén and T. R. Thomas, "Relationship of the plasticity index to machining parameters," *Int. J. Mach. Tools Manuf.*, vol. 41, pp. 2061–2069, Oct. 2001.

[21] R. D. Doherty *et al.*, "Current issues in recrystallization: A review," *Mater. Sci. Eng. A*, vol. 238, pp. 219–274, Nov. 1997.

[22] G. Gottstein, "Recovery, recrystallization, grain growth," in *Physical Foundations of Materials Science*. Berlin, Germany: Springer, 2004, pp. 303–356.

[23] L. M. Glarebrough, M. E. Hargreaves, and G. W. West, "The density of dislocations in compressed copper," *Acta Metall.*, vol. 5, pp. 738–740, Dec. 1957.
[24] K. Han, R. P. Walsh, A. Ishmaku, V. Toplosky, L. Brandao, and J. D. Embury, "High strength and high electrical conductivity bulk Cu," *Philos. Mag.*, vol. 84, no. 34, pp. 3705–3716, 2004.
[25] L. J. Cuddy, "Recovery of point defects in iron after low-temperature deformation," *Acta Metall.*, vol. 16, no. 1, pp. 23–28, 1968.
[26] M. C. Martin and K. F. Welton, "The change in electrical resistivity with plastic deformation of aluminum and nickel," *Acta Metall.*, vol. 15, no. 3, pp. 571–573, 1967.
[27] D. Lide, *CRC Handbook of Chemistry and Physics*, 88th ed. Boca Raton, FL, USA: CRC Press, 2007.
[28] P. S. Patil, R. K. Kawar, T. Seth, D. P. Amalnerkar, and P. S. Chigare, "Effect of substrate temperature on structural, electrical and optical properties of sprayed tin oxide (SnO_2) thin films," *Ceram. Int.*, vol. 29, no. 7, pp. 725–734, 2003.
[29] A. Kumar, G. Chandra, and O. P. Katyal, "The effect of grain boundary scattering on the electrical resistivity of polycrystalline lead, tin, and tin–lead alloy films," *Phys. Status Solidi A*, vol. 100, no. 1, pp. 169–175, 1987.
[30] T. Tamai, Y. Saitoh, S. Sawada, and Y. Hattori, "Peculiarities characteristics between contact trace and contact resistance of tin plated contacts," in *Proc. 54th IEEE Holm Conf. Elect. Contacts*, 2008, pp. 337–343.
[31] K. E. Trinh, "Laserinterferenztexturierung elektrischer Steckverbinder für die Automobilindustrie," (in German), Ph.D. dissertation, Dept. Mater. Sci. Eng., Saarland Univ., Saarbrücken, Germany, 2015. [Online]. Available: http://scidok.sulb.uni-saarland.de/volltexte/2015/6209/
[32] K. E. Trinh and F. Mücklich, *Laserinterferenzstrukturierung als Werkzeug zur Optimierung Elektrischer Steckverbinder*, (in German), vol. 71. Karlsruhe, Germany: VDE Fachbericht Kontaktverhalten Und Schalten, 2015, pp. 32–38.

K. E. Trinh, photograph and biography not available at the time of publication.

E. Ramos-Moore, photograph and biography not available at the time of publication.

I. Green, photograph and biography not available at the time of publication.

C. Pauly, photograph and biography not available at the time of publication.

M. Zamanzade, photograph and biography not available at the time of publication.

F. Mücklich, photograph and biography not available at the time of publication.